Comb-Actuated Resonant Torsional Microscanner With Mechanical Amplification

Aslihan Arslan, Dean Brown, Wyatt O. Davis, *Member, IEEE*, Sven Holmström, Sertan Kutal Gokce, *Student Member, IEEE*, and Hakan Urey, *Senior Member, IEEE*

***Abstract*—A comb-actuated torsional microscanner is developed for high-resolution laser-scanning display systems. Typical torsional comb-drive scanners have fingers placed around the perimeter of the scanning mirror. In contrast, the structure in this paper uses cascaded frames, where the comb fingers are placed on an outer drive frame, and the motion is transferred to the inner mirror frame with a mechanical gain. The structure works only in resonant mode without requiring any offset in the comb fingers, keeping the silicon-on-insulator-based process quite simple. The design intent is to improve actuator efficiency by removing the high-drag fingers from the high-velocity scanning mirror. Placing them on the lower velocity drive frame reduces their contribution to the damping torque. Furthermore, placement on the drive frame allows an increase of the number of fingers and their capacity to impart torque. The microscanner exhibits a parametric response, and as such, the maximum deflection is found when actuated at twice its natural frequency. Analytical formulas are given for the coupled-mode equations and frame deflections. A simple formula is derived for the mechanical-gain factor. For a 1-mm × 1.5-mm oblong scanning mirror, a 76° total optical scan angle is achieved at 21.8 kHz with 196-V peak-to-peak excitation voltages. [2009-0304]**

***Index Terms*—Comb drive, display, high-frequency scanning, mechanical coupling, torsional microscanner.**

I. Introduction

MICROSCANNERS are fundamental components in miniaturized systems for display [1], [3], imaging [4], [5], spectroscopy [6], barcode scanning [7], and telecommunication systems [8]. Microelectromechanical system (MEMS) scanners can meet the high-resolution, low-power consumption, and high-scanning speed requirements in such demanding applications. As an example, a Super Visual Graphics Array (SVGA) display requires a scan frequency $f > 20$ kHz and the product of the total optical scan angle (TOSA) θ_{OPT} and mirror size D to be $> 40^\circ \cdot$ mm [9]. Fig. 1(a) compares published scanner performances [10]–[26], [32] according to $\theta_{\mathrm{OPT}} \cdot D$-product and horizontal scan frequency f. The product $\theta_{\mathrm{OPT}} \cdot D \cdot f$ can be considered as a new figure of merit indicating the number of pixels per second. For electrostatic (ES) scanners with actuation voltage amplitude V, $\theta_{\mathrm{OPT}} \cdot D \cdot f/V$ can additionally be used as a metric to compare relative scanning efficiencies. Fig. 1(b) shows the ES scanner comparison using

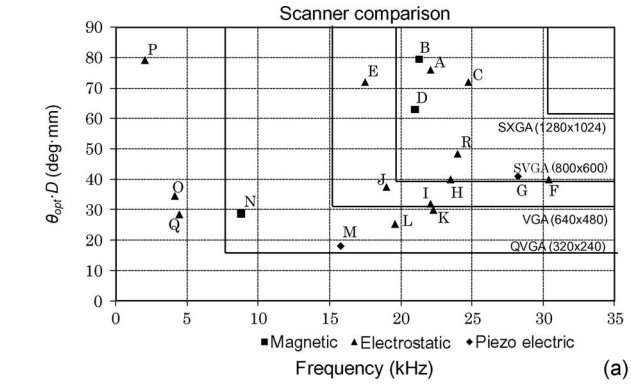

A) This work	B) Yalcinkaya [10]	C) Cho [11]	D)Torashima [12]
E) Urey [13]	F) Hsu [14]	G) Park [15]	H) Kuijpers [16, 17]
I) Ko [18]	J) Wine [19]	K) Yoda [20]	L) Ji [21]
M) Lebedev [22]	N) Ji [23]	O) Kim [24]	P) Jung [25]
Q) Milanovic [26]	R) Kurth [32]		

Fig. 1. (a) Microscanner-performance comparison based on the literature [10]–[26], [32]. Only high-performance scanners are reported and numbers in the plot area correspond to the reference listed below the figure. Triangle and square indicate ES- (J and R are parallel plate driven; all other ES scanners utilize comb drive) and EM-actuated scanners, respectively. The data for scanners J and L are acquired at reduced pressure. Scanners B and N are both 2-D scanners. Scanner B is also equipped with a position-feedback signal. Scanners G, M, and E are metallic; all others are made out of silicon. The solid lines indicate requirements for different display formats assuming 60-Hz refresh rate and bidirectional scanning, except for the HDTV line in the second chart, which assumes bidirectional scanning with two separate laser beams to reduce the frequency requirements. (b) Performance comparison of ES scanners according to two metrics: $\theta_{\mathrm{OPT}} \cdot D \cdot f$ and $\theta_{\mathrm{OPT}} \cdot D \cdot f/V$ [11], [18], [20][21], [25], [26], [32]. The former indicates the number of pixels per second, while the latter is an efficiency metric. The scanner presented here has a very high $\theta_{\mathrm{OPT}} \cdot D \cdot f$-product and, at the same time, one of the highest efficiencies [9].

Manuscript received December 3, 2009; revised March 23, 2010; accepted March 31, 2010. Date of publication June 7, 2010; date of current version July 30, 2010. Subject Editor G. Stemme.

A. Arslan, S. Holmström, S. K. Gokce, and H. Urey are with the Department of Electrical Engineering, Optical Microsystems Laboratory, Koç University, Istanbul 34450, Turkey (e-mail: aslihanarslan@gmail.com; sholmstrom@ku.edu.tr; sergokce@ku.edu.tr; hurey@ku.edu.tr).

D. Brown and W. O. Davis are with Microvision, Inc., Redmond, WA 98052 USA (e-mail: dean_brown@microvision.com; wyatt_davis@microvision.com).

Color versions of one or more of the figures in this paper are available online at http://ieeexplore.ieee.org.

Digital Object Identifier 10.1109/JMEMS.2010.2048095

those metrics. The scanner reported in this paper, marked as "A" in the figures, is among the highest performing devices in the literature and exceeds the frequency and scan-angle mirror-size requirements of SVGA and high-definition television (HDTV) display systems. There are additional requirements to make a dynamic display system, such as dynamic mirror deformation and angle sensors, in order to achieve diffraction-limited spot quality and high-precision pixel placement during scanning. Those additional requirements are not considered in this comparison. Best performing scanners are either electromagnetically (EM) or ES actuated.

EM-actuated 2-D scanners have been commercialized for picoprojector applications [3], [10]. EM scanners require the placement of magnets close to the scanning device, while ES comb-drive scanners have a fairly simple fabrication and arrangement of the actuator, with the tradeoff of requiring high voltage. ES-actuated scanners have been demonstrated by many groups [9], [11], [13], [14], [16], [18]–[20], [24]–[26], [32].

For ES-actuated resonant MEMS scanners, the performance is typically limited by the damping power losses at high frequencies and the small actuator capacitance of the structure due to limited perimeter area around the torsion mirror. In this paper, a mechanical-coupling principle is proposed to overcome these limitations. This paper presents results of modeling, fabrication, and characterization and demonstrates that this can be used to achieve very high performance scanning. Torsion scanners utilizing mechanical coupling to benefit from the aforementioned advantages were earlier demonstrated for EM actuation [10] and for a parallel-plate ES scheme [32].

II. Device Properties

The mechanically coupled comb-drive systems have two cascaded platforms, as shown in Fig. 2(a), referred to as the inner and outer frames, connected by the inner flexures. The device is anchored to the substrate via the outer flexures. Only the outer frame bears the ES comb-drive actuators, and the deflection of the outer frame is coupled to the inner frame. The inner frame is serving as the scanning mirror, and the role of the outer frame is to serve as the actuator. The main intended advantage of the arrangement compared with one without an outer frame (i.e., with the driving comb fingers attached directly to the mirror instead) is a reduced damping on the high-velocity mirror rotations. Experimental evidence for significant reductions in air damping of comb-drive scanning mirrors when the comb-finger gaps are increased has been shown in [30]. The design described in this paper takes such damping reduction to an extreme by removing the fingers completely from the high-velocity inner frame and transferring them to a lower velocity outer frame.

The outer-frame arrangement also allows one to increase the number of comb fingers compared with direct attachment of comb fingers to the mirror. Moreover, since the outer-frame rotation is only a fraction of the inner-frame rotation, the comb-finger disengagement can be managed such that the fingers impart ES torque to the oscillating system throughout the entire mirror-oscillation cycle, whereas for large-mirror rotations, the comb fingers directly attached to the mirror will be disengaged and unable to impart torque throughout a significant portion of the oscillation period.

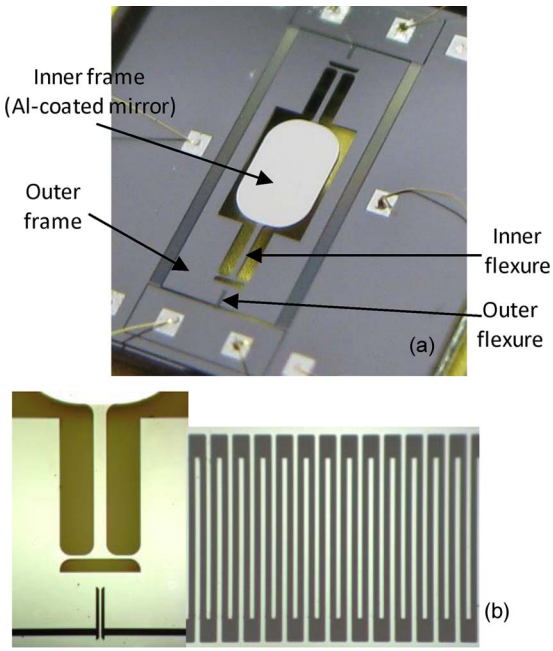

Fig. 2. (a) Picture of a full die. (b) Detail of inner and outer flexures and comb drive.

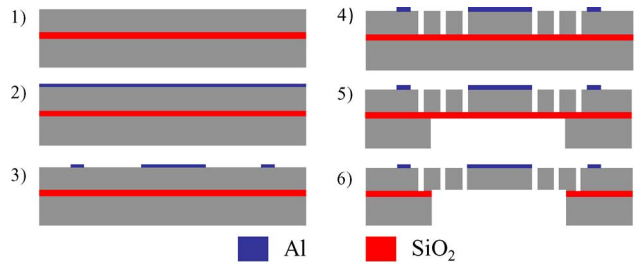

Fig. 3. Fabrication process of the novel comb-actuated torsional scanner.

The 50-μm-thick torsional scanner employs a 1-mm $\times$ 1.5-mm mirror. The inner frame is connected to the outer frame via two straight 750-μm-long and 70-μm-wide flexures extended along the y-axis. To fix the entire structure, another suspension system consisting of two straight flexures is used. The length and the width of these flexures are 280 and 13 μm, respectively. To lower peak stresses, the corners of both connection points of each flexure are rounded, and the inner flexures are fixed to the outer frame through a T-beam. The T-beam connection also helps to linearize the relationship between the elastic restoring torque and the deflection. The overall device size is 3.9 mm $\times$ 1.89 mm $\times$ 50 μm. Comb actuators are placed on both edges of the outer frame. In each comb set, individual combs are 5 μm wide and have a pitch of 20 μm.

The three-mask fabrication process is shown in Fig. 3. As starting material, silicon-on-insulator (SOI) wafers with a doped 50-μm-thick device layer are used [Fig. 3(1)]. To form the wire-bond electrodes and the mirror coating, Al is sputtered onto the device layer [Fig. 3(2)] and then patterned by photolithography using mask 1 [Fig. 3(3)]. Next, the device structures are defined through lithography with mask 2 and

front-side deep reactive-ion etch (DRIE) [Fig. 3(4)]. Mask 3 is now used to perform lithography for backside windowing. After the backside DRIE [Fig. 3(5)], the devices are released through etch of the buried oxide in HF vapor [Fig. 3(6)].

III. Analytical Modeling and FEA Results

A. Equation of Motion of the System

The two-degree-of-freedom (2-DoF) scanner is modeled using the Euler–Lagrange method, where potential and kinetic energies for each component in the system are inspected [10].

For the system shown in Fig. 2, θ_i and θ_o represent the mechanical scan angle of the inner and outer frames, and T_{EXT} is the total ES torque created at the comb fingers. The equations of motion of the coupled system are written as

$$\begin{aligned} J_i\ddot{\theta}_i + b_i\dot{\theta}_i + k_i(\theta_i - \theta_o) &= 0 \\ J_o\ddot{\theta}_o + b_o\dot{\theta}_o + (k_i + k_o)\theta_o &= T_{\mathrm{EXT}} + k_i\theta_i \end{aligned} \tag{1}$$

where J is the inertia, k is the spring constant, and b is the damping coefficient. The damping-coefficient and spring-constant parameters are assumed to be time independent in the analytical analysis of the system. The subscripts "i" and "o" denote the inner and the outer frames, respectively.

B. Mechanical-Coupling Principle

Unlike single-frame scanners, there are two torsion modes of interest in the two-frame scanners: one being out-of-phase (referred to as OP throughout this paper) and the other one being in-phase (referred to as IP throughout this paper) with respect to the two frames. In the scanner presented here, the inner frame bears no actuators, and a small movement of the outer frame is coupled into, and amplified at, the inner frame with a mechanical coupling gain (M). Fig. 4 shows the frequency response of the mechanically coupled systems with both magnitude and phase information. At lower vibration frequency, the inner and outer frames move in phase, whereas at higher vibration frequency, the frames move out of phase [2].

Large inner-frame-response amplitude can be obtained either at the IP-resonant mode [as in Fig. 4(a)] or the OP-resonant mode [as in Fig. 4(b)], depending on the mass and the spring constant of the inner and outer frames and flexures. Note that the largest mechanical gain between the inner and the outer frame is obtained in-between the two resonant modes where the outer-frame's frequency response is zero. However, the inner-frame deflection amplitude remains small compared with the resonant condition, rendering zero frequency an unsuitable operating point. Typical operating points of interest are the IP mode in Fig. 4(a) and OP mode in Fig. 4(b), where there is a mechanical gain.

The IP- and OP-resonance frequencies of the system are solved and represented by ω_{IP} and ω_{OP}

$$\omega_{\mathrm{IP}}^2 = \frac{k_i}{2J_o} + \frac{\omega_o^2}{2} + \frac{\omega_i^2}{2} - \Delta \tag{2}$$

$$\omega_{\mathrm{OP}}^2 = \frac{k_i}{2J_o} + \frac{\omega_o^2}{2} + \frac{\omega_i^2}{2} + \Delta \tag{3}$$

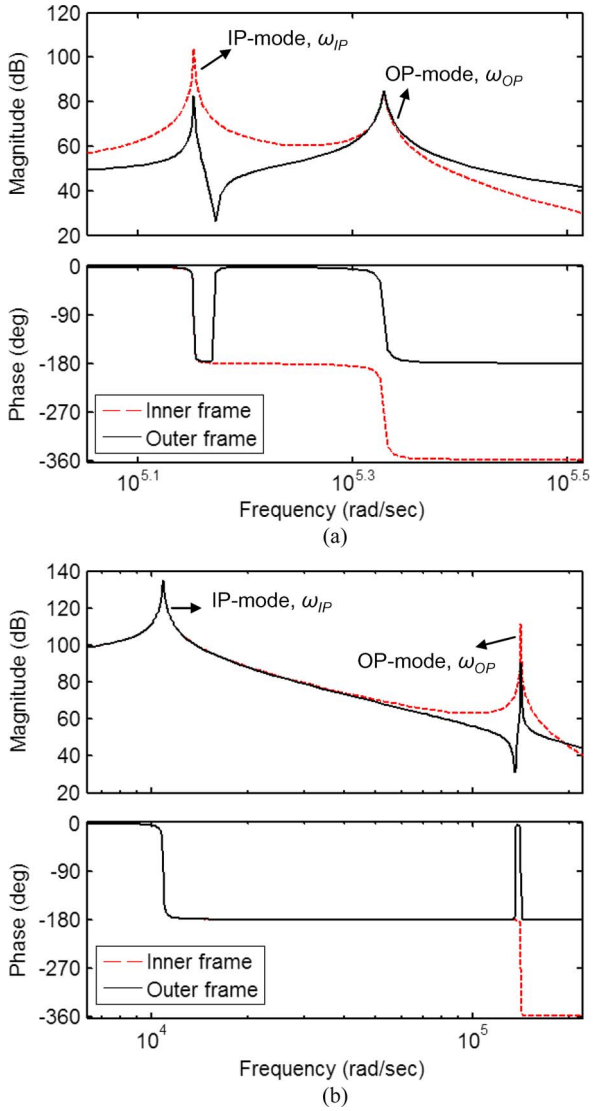

Fig. 4. Frequency and phase response of the coupled resonator system for two-frame systems. There are two cases of interest based on where the mechanical coupling $(M > 1)$ is obtained: (a) $M > 1$ in the IP mode and (b) $M > 1$ in the OP mode.

where

$$\Delta = \frac{\sqrt{-4k_ik_oJ_iJ_o + (k_oJ_i + k_iJ_i + k_iJ_o)^2}}{2J_iJ_o}. \tag{4}$$

The natural frequencies ω_i and ω_o of each frame acting alone are defined using the stiffness and inertia parameters of the inner and outer frames and given as

$$\omega_i = \sqrt{\frac{k_i}{J_i}} \quad \omega_o = \sqrt{\frac{k_o}{J_o}}. \tag{5}$$

The outer- and inner-frame rotational deflections can be solved in the Laplace domain for the 2-DoF system

$$\begin{aligned} &J_o\Theta_o(s)s^2 + b_o\Theta_o(s)s \\ &\quad + k_i\left(\Theta_o(s) - \Theta_i(s)\right) + k_o\Theta_0(s) = T_{\mathrm{EXT}} \end{aligned} \tag{6}$$

$$\begin{aligned} &J_i\Theta_i(s)s^2 + b_i\Theta_i(s)s \\ &\quad + k_i\left(\Theta_i(s) - \Theta_o(s)\right) = 0. \end{aligned} \tag{7}$$

The transfer functions of the coupled system are expressed as

$$\frac{\Theta_o(s)}{T_{\mathrm{EXT}}} = \frac{J_i s^2 + b_i s + k_i}{((J_o s^2 + b_o s + k_i + k_o)(J_i s^2 + b_i s + k_i) - k_i^2)} \tag{8}$$

$$\frac{\Theta_i(s)}{T_{\mathrm{EXT}}} = \frac{k_i}{((J_o s^2 + b_o s + k_i + k_o)(J_i s^2 + b_i s + k_i) - k_i^2)}. \tag{9}$$

Setting $s = j\omega$ for steady-state frequency-domain analysis, the frequency-dependent mechanical-coupling gain M is calculated by using (8) and (9) and shown as

$$M(\omega) = \left|\frac{\Theta_i(\omega)}{\Theta_o(\omega)}\right| = \frac{k_i}{\sqrt{(k_i - J_i\omega^2)^2 + (b_i\omega)^2}} \tag{10}$$

where ω is the vibration frequency. The numerically obtained IP and OP resonance frequencies are 1.7 kHz and 22.5 kHz, respectively. The mechanical-coupling gain of the scanner at ω_{OP} is calculated as 11 using (10).

Finite-element analysis (FEA) of the scanners is performed using ANSYS simulation tool. As shown in Fig. 5, at lower vibration frequency, the inner and outer frames move in phase and deflect by nearly the same amount. At higher vibration frequency, the respective motions of the inner and the outer frame are out of phase. Using the FEA, the out-of-phase resonance frequency of the device is found to be 22.5 kHz, and the corresponding mechanical coupling gain is 9. In the ANSYS simulations of the torsional scanners, comb actuators are modeled as additional inertial volumes on both sides of the device with smaller effective density in order to decrease the computational cost. The mechanical-coupling gain derived using the analytical formulas and the ANSYS results are not identical due to structural bending. The structural bending of the outer frame is apparent from the displacement contour plot in Fig. 5(b). This deformation will distort the collinearity of the comb fingers attached to the outer frame, which can be accounted for in the calculation of the actuating capacitance. Otherwise, the analytical formulas use a rigid-body assumption.

The presented device is designed to achieve 72° TOSA at its coupling frequency, and the parameters are adjusted to keep the maximum stress below 1.4 GPa [27] for the required deflection angle. As shown in Fig. 6, at the out-of-phase mode of the scanner, the stress is accumulated at the connection of the inner flexure to the outer frame. Using ANSYS, the maximum principal stress is found to be 1.2 GPa at 22.5 kHz for 72° TOSA.

The dynamic deformation of the mirror is not experimentally measured, but numerical modeling, as seen in Fig. 7, shows that it is too high for a commercial scanner. Work is continuing toward a design which can repeat this performance while keeping the dynamic mirror deformation below 10% of the utilized wavelength [31].

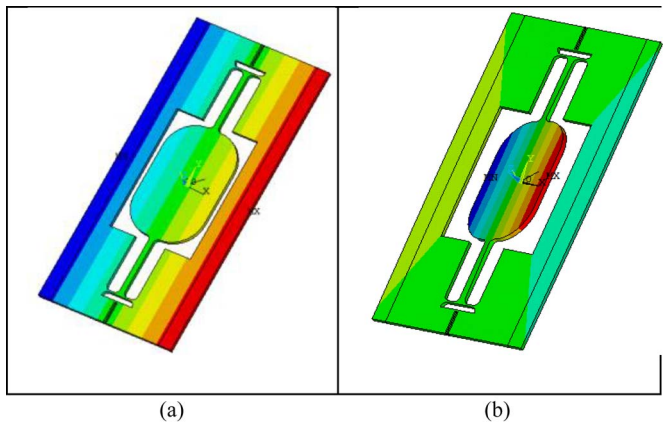

Fig. 5. Shape of the mechanical operation eigenmodes of the microscanner. (a) Lower vibration mode: The inner and outer frames move in phase with the same deflection amplitude. (b) Higher vibration mode: The outer frame and inner frame motions are out of phase with an amplitude ratio of 9.

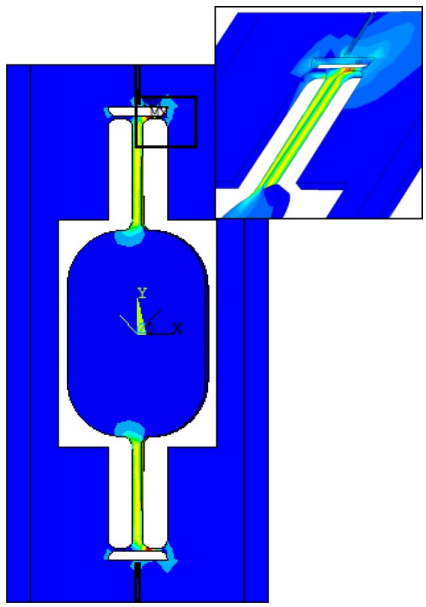

Fig. 6. Stress distribution of the torsional scanner. At the out-of-phase frequency of the scanner, stress is accumulated at the inner flexure and outer-frame connection, and the maximum principal stress is found to be 1.2 GPa for 72° TOSA.

IV. Characterization

A. Drive Characteristics of the Comb-Actuated Torsional Microscanners

The dynamic behavior of the comb-drive scanner varies with the excitation signal and can be modeled with the second-order differential equation given by (1). At the torsional mode, the capacitance varies with the angular deflection, and the ES torque depends on the displacement as well as the excitation voltage [28]. The actuation torque's dependence on displacement creates time-varying torsional stiffness, and the system is described by an equation of motion in the form of parametric nonlinear ordinary differential equations [27]–[29]. As seen in Figs. 8 and 9, the scanners exhibit spring-softening behavior, which is typical for ES scanners [14], [25].

Parametric oscillators have subharmonic oscillations which are located near $2f_r/n$, where f_r is the mechanical resonance

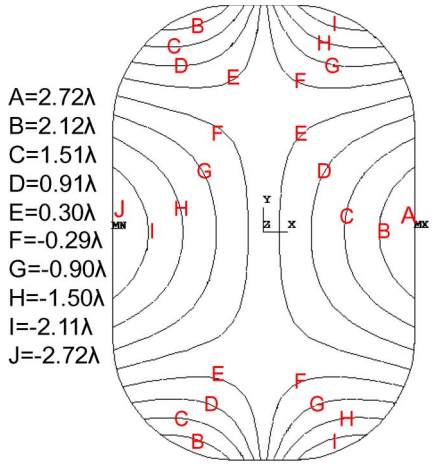

Fig. 7. ANSYS analysis of the dynamical warping of the mirror at 18° deflection. The deformation amplitude is expressed in multiples of the wavelength $\lambda = 510$ nm.

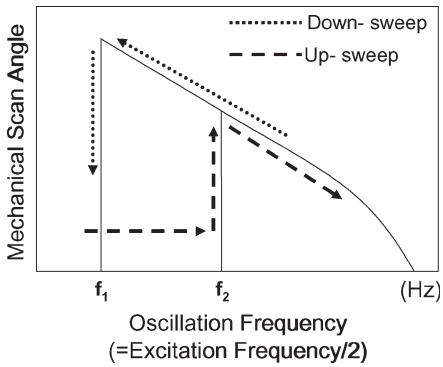

Fig. 8. Typical hysteretic frequency response of the nonlinear torsional scanner.

frequency of the system and n is a positive integer. The largest amplitude is obtained at $n = 1$, and it decreases with higher values of n, i.e., for maximum scan angle, the drive signal should be chosen as twice the mechanical resonance frequency [27].

Hysteretic frequency response is the other remarkable feature of the parametrically excited systems. Two different jump frequencies are obtained while the frequency is swept up and down, depending on the initial conditions [28], [29]. The frequency response of the parametric oscillator is shown in Fig. 8, and the mechanical jump frequencies are denoted by f_1 and f_2 $(f_1 < f_2)$. When the frequency is swept up, the oscillation starts at f_2, and the deflection angle decreases with further upsweep. The oscillation characteristic of the oscillator is different for the downsweep of the frequency. In this latter case, the mechanical deflection increases until f_1 and forms a peak. However, for even lower frequencies, the oscillations come to a full stop. Therefore, in order to obtain maximum scan amplitude, the scanner must be driven close to f_1. The region between two jump frequencies is unstable, where the maximum deflections are achieved by sweeping the frequency down from a stable point. The two boundary frequencies of the unstable region depend on the amplitude of the excitation voltage.

For different applied voltages, the range between the jump frequencies changes, and a tonguelike-shaped stability curve is obtained. The analytical investigation of the stability characteristics of the system is presented in [28]. The voltage-stability tongue shows the minimum required voltage for the oscillation where the two jump frequencies approach each other, and the unstable region in the frequency-response curve disappears.

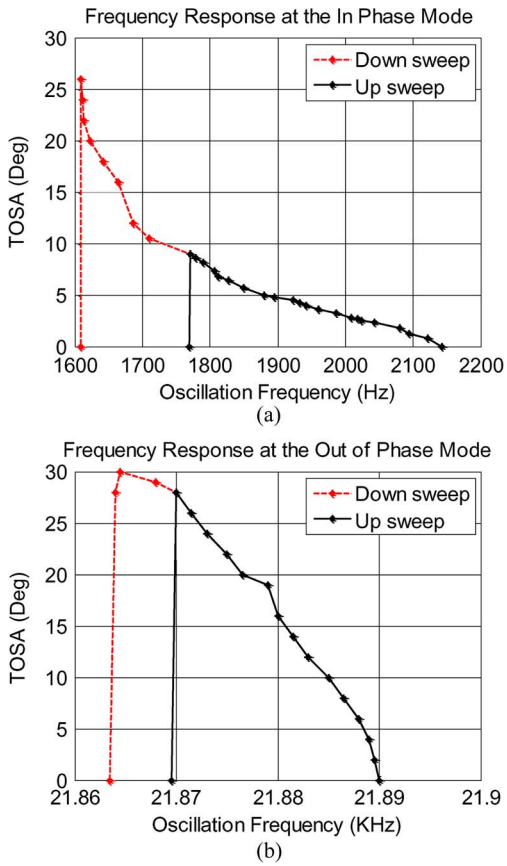

Fig. 9. Frequency response of Device 1. (a) In-phase mode. (b) Out-of-phase mode. The solid line represents the upsweep and the dashed line the frequency response of the downsweep.

B. Experimental Results

Comb-drive torsional-scanner designs are tested to validate the mechanical-coupling mechanism under ambient pressure and temperature conditions. All measurements referred to in this paper are performed using the following dc-biased sinusoid

$$V_{\text{drive}} = \frac{V_0}{2}(1 + \sin \omega t)$$

where V_0 is the peak-to-peak actuation voltage. This signal is applied to comb fingers placed on either side of the outer frame. In order to achieve the maximum angular rotation, the excitation signal is applied at frequencies equal to two times the in-phase and out-of-phase resonance frequencies of the torsional mode.

In this paper, experimental results of two torsional devices, denoted as Device 1 and Device 2, are presented. They are fabricated on different SOI wafers. Fig. 9(a) and (b) shows the frequency response of Device 1 at the in-phase and the out-of-phase resonance frequencies. The frequency responses of both torsional devices have the same hysteretic behavior. The results are obtained at 55 V_{pp} and 96 V_{pp} voltages for

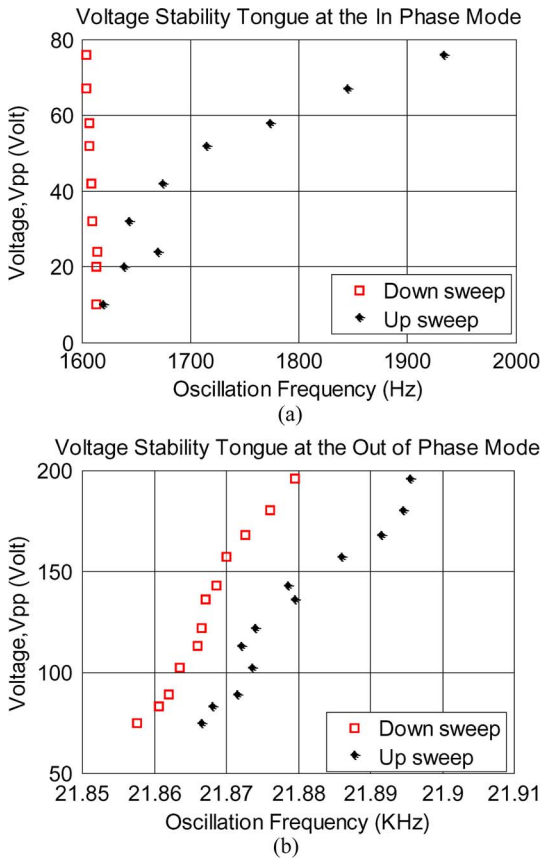

Fig. 10. Voltage-stability curve of Device 1. (a) In-phase mode. (b) Out-of-phase mode. Upsweep and downsweep jump frequencies (f_1 and f_2 in Fig. 8) are plotted with respect to drive voltages.

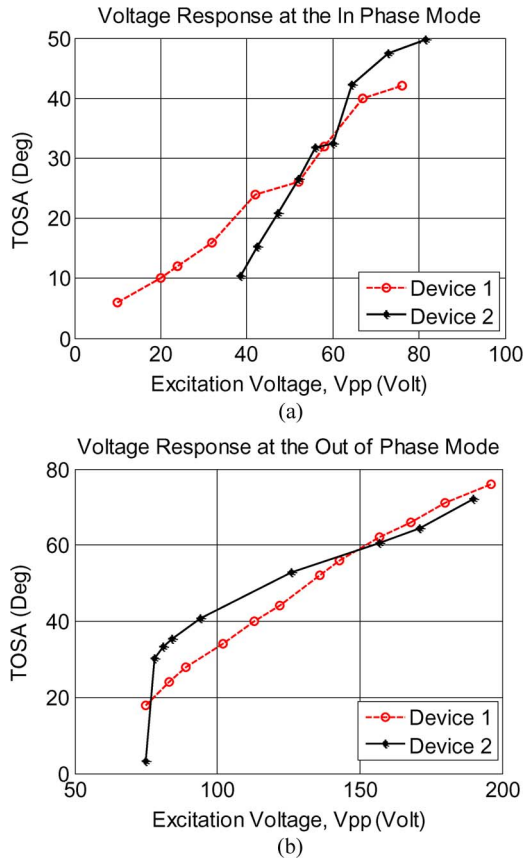

Fig. 11. Voltage response of Device 1 and Device 2. (a) In-phase mode. (b) Out-of-phase mode.

the corresponding modes. As shown in the figure, the in-phase and out-of-phase resonance frequencies are 1.6 and 21.8 kHz, respectively.

Voltage-stability tongues of Device 1 are obtained by actuating the scanner with different peak-to-peak voltages, and the experimentally obtained results of the in-phase and the out-of phase modes are shown in Fig. 10(a) and (b). Downsweep and upsweep frequencies represent f_1 and f_2, respectively. As shown in the figure, the stability boundary of the comb-drive torsional scanner varies with excitation voltage. The minimum voltage required to start the out-of-phase oscillation is found to be 75 $V_{\rm pp}$, and at the in-phase resonance mode, the oscillations start at 10-$V_{\rm pp}$ voltages.

The voltage response, illustrating the relationship between the maximum TOSA and the excitation voltage, is plotted for Device 1 and Device 2 and shown in Fig. 11. As discussed in the previous subsection, the maximum deflection is obtained at the downsweep frequency, and the corresponding inner-frame TOSA values are plotted in the figures. At the in-phase mode of Device 1, a 42° TOSA is obtained with 76 $V_{\rm pp}$ at 1.6 kHz, and the mechanical deflection of the inner and outer frames are equal. The out-of-phase frequency of the torsional mode is 21.8 kHz, and a 76° TOSA is obtained with 196 $V_{\rm pp}$ (Fig. 12). At this mode, the outer-frame deflection is amplified and transferred to the inner frame with a mechanical-coupling gain of about 8.5 (this includes an experimental measurement error of the outer-frame deflection) and agrees well with the ANSYS

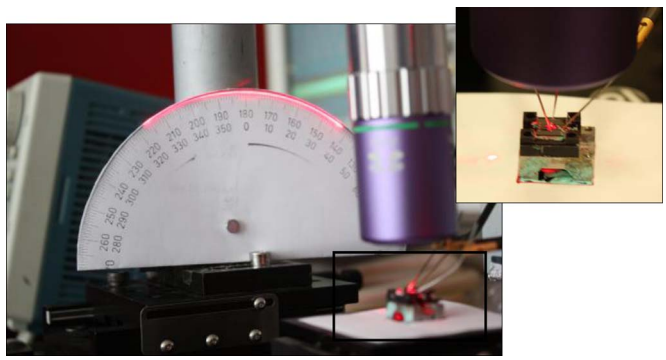

Fig. 12. Above scan line corresponds to 76° TOSA at 21.8 kHz.

results. The maximum deflection and the resonance frequencies of Device 2 are very close to Device 1 which is fabricated in a different fabrication run. A 50° TOSA is obtained with 81 $V_{\rm pp}$ at 1.6 kHz with Device 2. The out-of-phase frequency is 22.1 kHz in this case, and a 72° TOSA is obtained with 190 $V_{\rm pp}$ voltages. The experimentally obtained mechanical coupling gain is found to be 8.1.

V. Conclusion

A high-performance comb-drive resonant microscanner actuated with mechanical-coupling principle has been designed, fabricated, and tested. The device features two cascaded frames

where the comb actuators are placed around the edges of the outer frame. The inner frame bears no actuators and is actuated by mechanical amplification of the outer-frame motion. In the presented design, mechanical coupling is obtained at the out-of-phase resonance frequency of the system. The analytical formulas for the in-phase and out-of-phase resonance frequencies and the mechanical gain are derived and validated with FEA and experiments. The advantages of the mechanical-coupling principle compared with direct-drive scanners are the increased comb-finger area and larger torque arm, improved lateral stability due to shorter comb fingers, and reduced damping power loss at the combs due to limited motion of the outer frame combs. On the other hand, there is the added inertia of the outer frame and the additional design challenges due to other vibration modes. The scanner has one of the highest performance levels reported in the literature, indicating that the mechanical-coupling approach has some clear benefits. The achieved performance level is one of the highest in the MEMS scanner literature in terms of the product of mirror size (1 mm), TOSA (76°), and resonant frequency (21.8 kHz). At this performance level, the required voltage is 196 V_{pp}. As such, the scanner presented meets many of the challenges of dynamic displays. The aim of the work presented in this paper was to design a device for high-frequency scanning and high TOSA with a low $\theta_{\mathrm{OPT}} \cdot D \cdot f/V$-value in comparison with other devices in the literature. Getting also the dynamic deformation into the desired regime is an ongoing project but is not within the scope of this paper.

ACKNOWLEDGMENT

The authors would like to thank C. Hibert, N. Simonian, B. Lunardi, and J.-B. Bureau for contributions to the process development; P. Fluckiger and Y. Leblebici for support and help; and S. Olcer for help with photographs and setups. The microfabrication in this work was performed at the Center of Microtechnology (CMI), Ecole Polytechnique Federale de Lausanne (EPFL), Lausanne, Switzerland, with the support of the CMI staff.

REFERENCES

[1] A. Arslan, S. Holmstrom, S. K. Gokce, and H. Urey, "Comb-actuated resonant torsional scanner for microdisplays," in *Proc. IEEE/LEOS Int. Conf. Opt. MEMS Nanophoton.*, Clearwater, FL, 2009, pp. 139–140.

[2] A. Arslan, C. Ataman, S. Holmstrom, K. Hedsten, H. R. Seren, P. Enoksson, and H. Urey, "Mechanically coupled comb drive MEMS stages," in *Proc. IEEE/LEOS Int. Conf. Opt. MEMS Nanophoton.*, Freiburg, Germany, 2008, pp. 140–141.

[3] W. O. Davis, R. Sprague, and J. Miller, "MEMS-based pico projector display," in *Proc. IEEE/LEOS Int. Conf. Opt. MEMs Nanophoton.*, Freiburg, Germany, 2008, pp. 31–32.

[4] H. Ra, W. Piyawattanametha, Y. Taguchi, D. Lee, M. Mandella, and J. Solgaard, "Two-dimensional MEMS scanner for dual-axes confocal microscopy," *J. Microelectromech. Syst.*, vol. 16, no. 4, pp. 969–976, Aug. 2007.

[5] C. Chong, K. Isamoto, and H. Toshiyoshi, "Optically modulated MEMS scanning endoscope," *IEEE Photon. Technol. Lett.*, vol. 18, no. 1, pp. 133–135, Jan. 2006.

[6] C. Ataman, H. Urey, and A. Wolter, "A Fourier transform spectrometer using resonant vertical comb actuators," *J. Micromech. Microeng.*, vol. 16, no. 12, pp. 2517–2523, Oct. 2006.

[7] A. D. Yalcinkaya, O. Ergeneman, and H. Urey, "Polymer magnetic scanners for bar code applications," *Sens. Actuators A, Phys.*, vol. 135, no. 1, pp. 236–243, Mar. 2007.

[8] M. C. M. Lee, D. Hah, E. K. Lau, H. Toshiyoshi, and M. Wu, "MEMS-actuated photonic crystal switches," *IEEE Photon. Technol. Lett.*, vol. 18, no. 2, pp. 358–360, Jan. 2006.

[9] H. Urey, D. W. Wine, and T. D. Osborn, "Optical performance requirements for MEMS-scanner based microdisplays," *Proc. SPIE*, vol. 4178, pp. 176–185, 2000.

[10] A. D. Yalçýnkaya, H. Urey, D. Brown, T. Montague, and R. Sprague, "Two-axis electromagnetic microscanner for high resolution displays," *J. Microelectromech. Syst.*, vol. 15, no. 4, pp. 786–795, Aug. 2006.

[11] J. W. Cho, Y. H. Park, Y. C. Ko, B. L. Lee, S. J. Kang, S. W. Chung, W. K. Choi, Y. C. Cho, S. M. Chang, J. H. Lee, and J. Sunu, "Electrostatic 1D microscanner with vertical combs for HD resolution display," *Proc. SPIE*, vol. 6466, pp. 646 60B-1–646 60B-12, Jan. 2007.

[12] K. Torashima, T. Teshima, Y. Mizoguchi, S. Yasuda, T. Kato, Y. Shimda, and T. Yagi, "A micro scanner with low power consumption using double coil layers on a permalloy film," in *Proc. IEEE-LEOS Conf. Opt. MEMS*, Takamatsu City, Japan, 2004, pp. 192–193.

[13] H. Urey, "Torsional MEMS scanner design for high-resolution display systems," in *Proc. SPIE, Opt. Scanning II*, Seattle, WA, Jul. 2002, vol. 4773, pp. 27–37.

[14] S. Hsu, T. Klose, C. Drabe, and H. Schenk, "Fabrication and characterization of a dynamically flat high resolution micro-scanner," *J. Opt. A, Pure Appl. Opt.*, vol. 10, no. 4, pp. 1–8, Apr. 2008.

[15] J. H. Park, J. Akedo, and H. Sato, "High-speed metal-based optical microscanners using stainless-steel substrate and piezoelectric thick films prepared by aerosol deposition method," *Sens. Actuators A, Phys.*, vol. 135, no. 1, pp. 86–91, Mar. 2007.

[16] A. A. Kuijpers, D. Lierop, R. H. M. Sanders, J. Tangenberg, H. Moddejonge, J. W. T. Eikenbroek, T. S. J. Lammerink, and R. J. Wiegerink, "Towards embedded control for resonant scanning MEMS micromirror," in *Proc. Eurosensor XXIII*, Lausanne, Switzerland, 2009, pp. 1307–1310.

[17] A. A. Kuijpers, private communication, 2009.

[18] Y. C. Ko, J. W. Cho, Y. K. Mun, H. G. Jeong, W. K. Choi, J. W. Kim, Y. H. Park, J. B. Yoo, and J. H. Lee, "Eye-type scanning mirror with dual vertical combs for laser display," *Sens. Actuators A, Phys.*, vol. 126, no. 1, pp. 218–226, Jan. 2006.

[19] D. Wine, M. P. Helsel, L. Jenkins, H. Urey, and T. D. Osborn, "Performance of a biaxial MEMS-based scanner for microdisplay applications," *Proc. SPIE*, vol. 4178, pp. 186–196, Aug. 2000.

[20] M. Yoda, K. Isamoto, C. Chong, H. Ito, A. Murata, and H. Toshiyoshi, "Design and fabrication of a MEMS 1-D optical scanner using self-assembled vertical combs and scan-angle magnifying mechanism," in *Proc. IEEE-LEOS Conf. Opt. MEMS*, 2005, pp. 19–20.

[21] H. Ji, M. Cho, S. C. Kim, S. H. Lee, S. H. Kim, Y. Yee, and J. U. Bu, "An electrostatic scanning micromirror with diaphragm mirror plate and diamond-shaped reinforcement frame," *J. Micromech. Microeng.*, vol. 16, no. 5, pp. 1033–1039, Apr. 2006.

[22] M. Lebedev, H. Sato, and J. Akedo, "Optical micro-scanner fabricated on stainless steel by aerosol deposition method," in *Proc. IEEE Int. Conf. Ultrason., Ferroelectr., Freq. Control*, 2004, pp. 165–168.

[23] C. H. Ji, M. Choi, S. C. Kim, K. C. Song, J. U. Bu, and H. J. Nam, "Electromagnetic two-dimensional scanner using radial magnetic field," *J. Microelectromech. Syst.*, vol. 16, no. 4, pp. 989–996, Aug. 2007.

[24] J. Kim and L. Lin, "Electrostatic scanning micromirrors using localized plastic deformation of silicon," *J. Micromech. Microeng.*, vol. 15, no. 9, pp. 1777–1785, Jul. 2005.

[25] I. W. Jung, S. Kim, and O. Solgaard, "High-reflectivity broadband photonic crystal mirror MEMS scanner with low dependence on incident angle and polarization," *J. Microelectromech. Syst.*, vol. 18, no. 4, pp. 924–932, Aug. 2009.

[26] V. Milanovic, G. A. Matus, and D. T. McCormic, "Gimbal-less monolithic silicon actuators for tip–tilt-piston micromirror applications," *IEEE J. Sel. Topics Quantum Electron.*, vol. 10, no. 3, pp. 462–471, May/Jun. 2004.

[27] A. Wolter, H. Schenk, H. Korth, and H. Lakner, "Torsional stress, fatigue and fracture strength in silicon hinges of a micro scanning mirror," *Proc. SPIE*, vol. 5343, pp. 176–185, Dec. 2004.

[28] C. Ataman and H. Urey, "Modeling and characterization of comb-actuated resonant microscanners," *J. Micromech. Microeng.*, vol. 16, no. 1, pp. 9–16, Jan. 2006.

[29] K. L. Turner, S. A. Miller, P. G. Hartwell, N. C. MacDonald, S. H. Strogatz, and S. G. Adams, "Five parametric resonances in a microelectromechanical system," *Nature*, vol. 396, no. 6707, pp. 149–152, Nov. 1998.

[30] T. Sandner, T. Klose, A. Wolter, H. Schenk, H. Lakner, and W. Davis, "Damping analysis and measurement for a comb-drive scanning mirror," *Proc. SPIE*, vol. 5455, pp. 147–158, Aug. 2004.
[31] H. Urey and D. Dickensheets, "Display and imaging systems," in *MOEMS and Applications*, E. Motamedi, Ed. Bellingham, WA: SPIE, 2005, ch. 8.
[32] S. Kurth, C. Kaufmann, R. Hahn, J. Mehner, W. Doetzel, and T. Gessner, "A novel 24-kHz resonant scanner for high-resolution laser display," in *Proc. SPIE, MOEMS Display Imaging Syst. III*, Bellingham, WA, 2005, vol. 5721, pp. 23–33.

Aslihan Arslan received the B.Sc. degree in physics from Middle East Technical University, Ankara, Turkey, and the M.Sc. degree in electrical and computer engineering from Optical Microsystems Laboratory, Koç University, Istanbul, Turkey, in 2008.

She has been with Optical Microsystems Laboratory, Koç University, since she worked as Graduate Research and Teaching Assistant for her M.Sc degree.

Dean Brown received the BSME degree from the University of California, Santa Barbara, in 1974.

He was with Bunker-Ramo and Honeywell in ocean systems technology from 1974 to 1981, developing deep-water packaging and deployment systems for sonobuoys and mechanical systems for a submersible ROV. From 1981 to 1997, he was with Chem-Nuclear Systems, JLR Computer Analysis and Packaging Technology, where he performed advanced design analyses of mechanical systems in a variety of industries, including chemical and radioactive waste handling, electronics packaging, magnetic systems, heavy trucking, nuclear fuel rod and power plant systems, lifting and handling equipment, marine systems, tunnel-boring equipment, paper-mill equipment, and sports and fitness equipment. Since 1997, he has been with Microvision, Inc., Redmond, WA, where he has designed and analyzed silicon MEMS devices, including gyroscopic sensors and scanning mirrors. He is a coinventor of nine patents related to MEMS scanning mirrors.

Wyatt O. Davis (M'08) received the B.S. and M.S. degrees in mechanical engineering from Washington State University in 1993 and 1995, respectively, and the Ph.D. degree in mechanical engineering from the University of California, Berkeley in 2001.

From 2001 to 2003, he was MEMS Engineer with Onix Microsystems, Richmond, CA. Since 2003, he has been with Microvision, Inc., Redmond, WA, where he is currently a Principal Engineer, developing MEMS subsystems for display and imaging applications. He is the holder of nine issued patents.

Sven Holmström received his M.Sc. in engineering biology from Linköping University, Sweden in 2005.

Since November 2005, he has been a Research Engineer with the Optical Microsystems Laboratory, Koç University, Istanbul, Turkey. His research interests include micro- and macroscanner applications and MEMS fabrication.

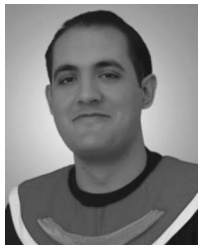

Sertan Kutal Gokce (S'06) received the B.Sc. degrees in electrical and electronics engineering from Middle East Technical University, Ankara, Turkey in 2008. He is currently working toward the M.S. degree at Koç University, Istanbul, Turkey, working with H. Urey.

His current research focus is FEM design and microfabrication of MEMS-based scanners. His research interests are microsystems and MEMS structures for biological and optical applications.

Hakan Urey (M'92–SM'09) received the B.S. degree in electrical engineering from Middle East Technical University, Ankara, Turkey, in 1992, and the M.S. and Ph.D. degrees in electrical engineering from Georgia Institute of Technology, Atlanta, in 1996 and 1997.

After completing his Ph.D., he was with Microvision Inc., Seattle, as Research Engineer, and he played a key role in the development of the scanning display technologies. He was the Principal System Engineer when he left Microvision to join the faculty of engineering, Koç University, Istanbul, Turkey, where he established the Optical Microsystems Research Laboratory. He is currently an Associate Professor of electrical engineering with Koç University. He has published more than 100 journal and conference papers, six edited books, two book chapters, and he is the holder of 18 issued and several pending patents. His research interests are in optical MEMS, optical system design, and laser-based 2-D/3-D display and imaging systems.